Research Article

Nano Research
2024, 17(4): 2528–2537

ISSN 1998-0124 CN 11-5974/O4
https://doi.org/10.1007/s12274-023-6206-9

Chalcogen-dependent catalytic properties of RuX_2 (X = S/Se/Te) nanoparticles decorated carbon nanofibers for hydrogen evolution in acidic and alkaline media

Chengkai He[1], Yue Wei[1], Jia Xu[2], Yujie Wei[1], Tao Wang[1], Rongfei Liu[3], Lvlv Ji[1] (✉), Zhun Liu[2] (✉), and Sheng Wang[1] (✉)

[1] School of Materials Science and Engineering, Zhejiang Sci-Tech University, Hangzhou 310018, China
[2] Department of Physics, Shaoxing University, Shaoxing 312000, China
[3] Zhejiang Kangjiesi New Material Technology Co., LTD, Zhuji 311800, China

Received: 5 July 2023 / **Revised:** 13 August 2023 / **Accepted:** 17 September 2023

ABSTRACT

Transition metal dichalcogenides (TMDs), with the general formula MX_2 (M = Mo/W/Fe/Co/Ni, etc.; X = S/Se/Te), have attracted extensive research interests for hydrogen evolution reaction (HER). Compared with numerous studies on noble-metal-free TMDs, the chalcogen-dependent HER catalytic properties of noble-metal-based TMDs are lack of sufficient research attention. Herein, a facile electrospinning-assisted synthetic strategy is proposed to synthesize ruthenium dichalcogenides (RuX_2, X = S/Se/Te) nanoparticles decorated carbon nanofibers (CNFs). Benefiting from the identical nanofibrous morphology and exposed crystal planes of RuX_2 (111), the catalytic activities of RuX_2@CNFs samples were investigated and compared in a fair and direct manner. Detailed electrochemical measurements coupled with density functional theory calculations were carried out to probe their intrinsic HER catalytic activities, resulting in the catalytic activity order of RuS_2@CNFs > $RuSe_2$@CNFs > $RuTe_2$@CNFs in acidic media and that of RuS_2@CNFs > $RuTe_2$@CNFs > $RuSe_2$@CNFs in alkaline media. The superior catalytic performance of RuS_2@CNFs mainly stems from the relative lower HER energy barriers and thereby the higher intrinsic catalytic activity of RuS_2 (111), leading to ultralow overpotentials of 44 and 9 mV at 10 mA·cm^{-2} in acidic and alkaline media, respectively. $RuSe_2$ (111) is endowed with the more optimized Gibbs free energy of hydrogen adsorption (ΔG_{H^*}) than $RuTe_2$ (111), but $RuTe_2$ (111) shows enhanced catalytic property for H_2O dissociation and OH^- desorption than $RuSe_2$ (111), therefore, resulting in the altered catalytic activity sequences for $RuSe_2$ and $RuTe_2$ in acidic and alkaline media.

KEYWORDS

hydrogen evolution reaction, transition metal dichalcogenides, carbon nanofibers, electrocatalysis, catalytic activity

1 Introduction

The global energy crisis and environment pollution have triggered the development of renewable energy to replace the traditional fossil fuels [1]. Hydrogen, a kind of green energy carrier with zero-carbon content, is recognized as the most promising alternative to traditional fossil fuels [2–4]. Electrochemical water splitting, driven by sustainable energy sources (such as solar, wind, and water energies), is the most promising pathway to produce high-purity hydrogen in an environmental-friendly manner [5]. Hydrogen evolution reaction (HER) and oxygen evolution reaction (OER) are the two half reactions of water splitting, but the sluggish kinetics of HER and OER lead to large overpotential and small current density [6–8]. Therefore, highly efficient electrocatalysts are indispensable to minimize the overpotential and save the electricity cost [9–11]. To date, Pt-based materials are recognized as the most efficient HER electrocatalysts, but the resource scarcity and high cost of Pt impede their practical applications [12–14].

In the past decade, a variety of electrocatalysts including transition metal chalcogenides, phosphides, carbides, nitrides, and borides were exploited and evaluated toward HER [15–17]. Owing to the unique physicochemical properties such as tunable electronic structures, sizable bandgaps, and adjustable dimensionalities, transition metal dichalcogenides (TMDs) with the general formula MX_2 (M = Mo/W/Fe/Co/Ni, etc.; X = S/Se/Te) have attracted extensive research interests for HER [18–20]. Previous studies demonstrated that the chalcogen ligands played crucial roles in regulating the electronic structure and electrical conductivity of TMDs, as well as their HER catalytic properties in different electrolytes [21–24]. For instance, Shen and coworkers revealed that the HER catalytic activities of Ni dichalcogenides were remarkably influenced by chalcogen ligands, and the catalytic activity order was $NiSe_2$ > NiS_2 > $NiTe_2$ in both acidic and alkaline media [22]. In another study, Chang and coworkers demonstrated the higher catalytic activity of 1T'-WTe_2 than 2H-WS_2 and 2H-WSe_2 in 0.5 M H_2SO_4, which was mainly attributed to the higher conductivity of semimetallic 1T'-phase-stable WTe_2 with a one or two order higher of charge-transfer rate [23]. To date, a vast majority of investigations are focused on the

Address correspondence to Lvlv Ji, llji@zstu.edu.cn; Zhun Liu, liu6zhun@163.com; Sheng Wang, wangsheng@zstu.edu.cn

清華大學出版社 Tsinghua University Press Springer

design and synthesis of nonnoble-metal-based (such as Mo, W, Fe, Co, and Ni) dichalcogenides for HER. Although significant advances have been made, the HER catalytic activities of these noble-metal-free TMDs are still far inferior to Pt-based materials. In contrast, other family members of TMDs (for example, non-Pt noble-metal-based TMDs) are lack of sufficient research attention, not to mention their chalcogen-dependent catalytic properties for HER in acidic and alkaline media.

In Pt-group metals, Ru shows a relatively much lower price (~ 4% of Pt), but possesses a Pt-like hydrogen bonding strength (~ 65 kcal·mol^{-1}) [25, 26]. In recent years, Ru-based dichalcogenides (RuX_2, X = S/Se/Te) have received increasing research interests for water splitting [27–29]. For example, Mu and coworkers investigated the HER and OER catalytic performances of the laminar Ru/RuS_2 heterostructure in acidic media, revealing its interfacial charge rearrangement and conductivity enhancement for efficient electrocatalysis [27]. Luo and coworkers reported the synthesis of hexagonal $RuSe_2$ nanosheets with a mixture of 2H and 1T phases, which exhibited Pt-like HER catalytic performance in alkaline and neutral media [28]. Feng and coworkers revealed that the high crystalline $RuTe_2$ nanoparticles decorated graphene can afford outstanding bifunctional catalytic performance for HER and OER in 1 M KOH [29]. Despite these individual studies on uncovering the excellent catalytic activities of RuX_2, Li and coworkers have attempted to explore the HER catalytic performances of RuX_2 through experimental and theoretical investigations [30]. However, the as-prepared RuX_2 samples exhibited multiple exposed crystal planes and their intrinsic catalytic activities have not been further compared by the normalization of the electrochemical active surface areas (ECSAs). Therefore, it remains challenging to make direct and fair comparisons of the intrinsic HER activities for pure-phase RuX_2 on an equal footing. An intensive experimental and theoretical study is still required to reveal the chalcogen-dependent intrinsic catalytic properties of RuX_2 with specific exposed crystal planes in acidic and alkaline media.

The HER catalytic performance is also affected by the number of accessible active site. In this regard, dispersing catalytic active RuX_2 nanoparticles on conductive carbon nanomaterials is an effective strategy. Among various carbon nanostructures, one-dimensional (1D) carbon nanostructures are endowed with advantageous properties, featuring in providing abundant active sites in the radial direction and benefitting rapid electron transfer along the axial direction [31]. These 1D structured carbon nanomaterials can interconnect with each other to form a porous catalytic network, thereby facilitating the electrolyte penetration and gas emission [32].

In this study, an electrospinning-assisted synthetic strategy was applied to prepare a series of RuX_2 (X = S/Se/Te) nanoparticles *in situ* embedded in carbon nanofibers (CNFs), which were respectively denoted as RuS_2@CNFs, $RuSe_2$@CNFs, and $RuTe_2$@CNFs. The as-prepared RuX_2@CNFs catalysts possess the identical nanofibrous morphology and specific exposed crystal planes of RuX_2 (111), which make it reasonable to achieve a fair and direct comparison for relevant catalytic activities. The electrochemical measurements reveal the HER catalytic activity order of RuS_2@CNFs > $RuSe_2$@CNFs > $RuTe_2$@CNFs in 0.5 M H_2SO_4, whereas the activity sequence is changed as RuS_2@CNFs > $RuTe_2$@CNFs > $RuSe_2$@CNFs in 1 M KOH. Density functional theory (DFT) calculations provide a comprehensive analysis of the chalcogen-dependent catalytic properties of RuX_2 (111) by regarding their HER energy barriers, which are in great agreement with the experimental catalytic orders of RuX_2@CNFs samples in acidic and alkaline media. In addition, their electrical conductivities are also analyzed to reveal the crucial roles of chalcogen ligands. The optimal sample RuS_2@CNFs shows ultralow overpotentials of 44 and 9 mV to achieve the current density of 10 mA·cm^{-2} in acidic and alkaline media, respectively, which are comparable or superior to the commercial 20% Pt/C and the recently reported Ru-based catalysts.

2 Experimental

2.1 Reagents

Ruthenium chloride trihydrate (98%, $RuCl_3·3H_2O$), sulfur, selenium, and tellurium powders were purchased from Macklin Reagents Ltd. Polyacrylonitrile (PAN, M_W = 150,000), 20% Pt/C, and *N*,*N*-dimethylformamide (> 99.5%, DMF) were purchased from Sigma-Aldrich Co. High-purity air and argon (99.999%) gases were purchased from Hangzhou Gases Co. All other chemical reagents were of analytical grade and used as received without further purification. All electrolyte solutions were prepared with Milli-Q ultrapure water (> 18 MΩ·cm).

2.2 Synthesis of $RuCl_3$@PAN nanofibers

$RuCl_3$@PAN nanofibers were synthesized by the electrospinning method. Typically, $RuCl_3·3H_2O$ (0.5 mmol) and PAN (1 g) were dissolved in DMF (9 mL) by magnetic stirring to obtain the homogeneous solution. After that, the mixed solution was loaded into a plastic syringe equipped with a stainless-steel needle. A revolving Al foil was used for collecting the electrospun nanofibers, and the distance between the needle tip and Al foil was set as 20 cm. The solution feeding speed was set as 0.25 mL·h^{-1}, and a high voltage of 13 kV was applied between the needle and Al foil to trigger the electrospinning. During the electrospinning, the humidity and temperature were controlled at around 38% and 25 °C, respectively. After the electrospinning for 12 h, the obtained $RuCl_3$@PAN nanofibers were dried in a vacuum oven at 60 °C for 12 h. In the parallel experiments, other two reference samples of $RuCl_3$@PAN-0.25 and $RuCl_3$@PAN-1 were obtained under identical conditions except that the feeding contents of $RuCl_3·3H_2O$ were 0.25 and 1 mmol, respectively.

2.3 Synthesis of Ru@CNFs

To synthesize Ru@CNFs, $RuCl_3$@PAN nanofibers were first pre-oxidized at 270 °C in the air for 1 h with a heating rate of 1 °C·min^{-1}, followed by the carbonization at 800 °C for 2 h in the Ar atmosphere with a heating rate of 2 °C·min^{-1}. In the parallel experiments, reference samples of Ru@CNFs-0.25 and Ru@CNFs-1 were obtained under identical conditions except that the precursor samples were $RuCl_3$@PAN-0.25 and $RuCl_3$@PAN-1, respectively.

2.4 Synthesis of RuS_2@CNFs, $RuSe_2$@CNFs, and $RuTe_2$@CNFs

To synthesize RuX_2@CNFs (X = S/Se/Te), X powder (720 mg) and Ru@CNFs (12 mg) were placed at separate positions in a porcelain boat with X powder at the upstream side of the tube furnace. The samples were pyrolyzed at 700 °C for 2 h in the Ar atmosphere with a heating rate of 3 °C·min^{-1}. In the parallel experiments, reference samples of RuS_2@CNFs-600 and RuS_2@CNFs-800 were obtained under identical conditions of RuS_2@CNFs except that pyrolysis temperatures were 600 and 800 °C, respectively. In addition, reference samples of RuS_2@CNFs-0.25 and RuS_2@CNFs-1 were obtained under identical conditions of RuS_2@CNFs except that the precursor samples were Ru@CNFs-0.25 and Ru@CNFs-1, respectively.

2.5 Characterizations

Fourier transform infrared (FT-IR) spectra were obtained on a Nicolet 6700 spectrometer (Thermo Fisher Nicolet, USA) with KBr pellets. X-ray diffraction (XRD) patterns were obtained on a Rigaku D/max-2200 via ceramic monochromatized Cu-Kα radiation (λ = 0.154 nm) operating at 40 kV and 40 mA. Raman spectra were obtained on a confocal microscope laser Raman spectrometer (Renishaw inVia). Scanning electron microscopy (SEM) images and energy-dispersive X-ray spectrometer (EDX) spectra were recorded at ZEISS VLTRA-55 equipped with a Horiba EDX system. SEM images and EDX spectra were recorded under the voltage of 3 and 10 kV, respectively. Transmission electron microscopy (TEM) and high-resolution TEM (HRTEM) images were recorded on JEM-2010 HR. X-ray photoelectron spectroscopy (XPS) spectra were recorded on a Kratos Axis Ultra DLD X-ray Photoelectron Spectrometer with 100 W monochromatic Al-Kα radiation as the X-ray excitation source. The C 1s peak (284.6 eV) was used for internal calibration, and the peak fitting was processed by the XPS Peak 41 software. The Brunauer–Emmett–Teller (BET) surface areas were measured on a Quanta Chrome Nova 2200e by N_2 adsorption at 77.4 K. The samples were degassed at 300 °C for 3 h before measurements.

2.6 Electrochemical measurements

Electrochemical measurements were conducted on the electrochemical workstation (CHI 660E, Chenhua, China) with a standard three-electrode setup, consisting of a working electrode (glassy carbon electrode, GCE), a counter electrode (carbon rod), and a reference electrode (saturated calomel electrode, SCE). To prepare the working electrode, electrocatalyst (4 mg) and Nafion solution (5 wt.%, 80 μL) were first dispersed in 1 mL of 4:1 (*v*/*v*) water/ethanol. After that, the resultant suspension (5 μL) was dropped onto the surface of GCE (mass loading: ~ 0.26 mg·cm^{-2}), followed by drying at room temperature.

The HER catalytic performances of electrocatalysts were evaluated in N_2-saturated 0.5 M H_2SO_4 and 1 M KOH. The reported potentials were referred to the reversible hydrogen electrode (RHE) via the Nernst equation $E_{RHE} = E_{SCE} + 0.059pH + 0.244$, which were experimentally calibrated considering RHE in the high-purity H_2-saturated electrolyte with a polished Pt sheet as the working electrode. In 0.5 M H_2SO_4, $E_{RHE} = E_{SCE} + 0.273$ V; in 1 M KOH, $E_{RHE} = E_{SCE} + 1.05$ V. Unless stated otherwise, linear sweep voltammetry (LSV) was conducted at a scan rate of 2 mV·s^{-1}. The Tafel slope was obtained from the LSV curves using a linear fit applied to the points in the Tafel region. Electrochemical impedance spectroscopy (EIS) measurements were conducted from 10^{-2} to 10^5 Hz with an amplitude of 5 mV at the applied potentials. The electrochemical stability measurements were conducted by cyclic voltammetry (CV) scanning and long-term electrolysis. To evaluate the electrochemical double-layer capacitance (C_{dl}) of the electrocatalysts, CV scanning with different scan rates was conducted within the potential range of 0–0.2 V vs. RHE in 1 M KOH. Unless stated otherwise, LSV and Tafel data plots were corrected with 90% *iR* compensation. The electrochemical measurements were all performed at 22 ± 2 °C.

2.7 DFT calculations

All DFT calculations were conducted by using the projector augmented wave method as implemented in the Vienna ab-initio simulation package (VASP). A cutoff kinetic energy of 520 eV for the plane-wave basis set was applied, and a 4 × 4 × 1 *k*-point grid was chosen to integrate the Brillouin zone. The Perdew–Burke–Ernzerh functional was performed within the generalized gradient approximation. The structures were optimized with the iterative convergence of energy and force of 10^{-6} eV and 0.01 eV·Å^{-1}, respectively.

The surface adsorption models were built based on the RuS_2 (111), $RuSe_2$ (111), and $RuTe_2$ (111) planes in line with the exposed (111) crystal planes in HRTEM images. A vacuum space of 20 Å was applied along the *z*-direction to avoid periodic interactions. During optimization, the atoms from the bottom to the middle layer were fixed, and the upper two adjacent layers were free for relaxation. The adsorption energies of various intermediates in HER were explored to assess the theoretical activity.

HER reaction pathways in acidic media are listed as follows

$$^* + H^+ + e^- \rightarrow H^* \text{ (Volmer step)} \quad (1)$$

$$2H^* \rightarrow H_2 + 2^* \text{ (Tafel step)} \quad (2)$$

$$H^* + H^+ + e^- \rightarrow H_2 + ^* \text{ (Heyrovsky step)} \quad (3)$$

where, * indicates a reaction site and H* presents the H atom absorbed on the active site. The change in Gibbs free energy (ΔG) of each adsorbed intermediate was calculated based on the computational hydrogen electrode method. At standard condition (T = 298.15 K, pH = 0, and U = 0 V vs. standard hydrogen electrode (SHE)), the adsorption free energy of H* can be deduced based on

$$\Delta G_{H^*} = \Delta E_{H^*} + \Delta E_{ZPE} - T\Delta S = E(H^*) - E(^*) - E(H_2)/2 + \Delta E_{ZPE} - T\Delta S \quad (4)$$

HER reaction pathways in alkaline media are listed as follows

$$^* + H_2O + e^- \rightarrow H^* + OH^- \text{ (Volmer step)} \quad (5)$$

$$2H^* \rightarrow H_2 + 2^* \text{ (Tafel step)} \quad (6)$$

$$H^* + H_2O + e^- \rightarrow H_2 + ^* + OH^- \text{ (Heyrovsky step)} \quad (7)$$

In alkaline media, the HER electrocatalysis involved a multi-step process including adsorption of H_2O, dissociation of H_2O, desorption of OH^-, and desorption of generated H_2. Therefore, the detailed alkaline HER electrocatalysis follows the following steps

$$^* + H_2O + e^- \rightarrow H_2O^* + e^- \rightarrow (H-OH)^* + e^- \rightarrow H^* + OH^- \rightarrow 1/2H_2 + ^* + OH^- \quad (8)$$

The exact free energy of OH^- was difficult to calculate while the free energy of OH^- was required, so a correction factor of $\Delta G_{(OH^-)-(OH^*)}$ has been introduced to describe the free energy difference between OH^- and OH* in the bi-layer configuration as

$$\Delta G_{(OH^-)-(OH^*)} = G_{(^*+1/2H_2+OH^-)} - G_{(OH^*)} - 1/2G_{(H_2)} = G_{(^*+H_2O)} - G_{(OH^*)} - 1/2G_{(H_2)} \quad (9)$$

in which the reaction Gibbs free energy (G) is defined as

$$G = E + E_{ZPE} - TS \quad (10)$$

where, E is the binding energy and T is the temperature (T = 298.15 K). E_{ZPE} and S are the difference in zero-point energy and entropy change, respectively. Afterwards, the free energy of the adsorbed state ($H^* + OH^-$) can be calculated as

$$\Delta G = \Delta E + \Delta E_{ZPE} - T\Delta S + \Delta G_{(OH^-)-(OH^*)} \quad (11)$$

3 Results and discussion

3.1 Synthesis and characterization of the RuX_2@CNFs catalysts

Scheme 1 shows the schematic synthetic route for RuX_2@CNFs. Briefly, $RuCl_3·3H_2O$ and PAN were first dissolved in DMF, and the mixed solution was then electrospun to fabricate the hybrid $RuCl_3$@PAN nanofibers. After experiencing the pre-oxidation at 270 °C in the air and the following carbonization at 800 °C under an Ar atmosphere, $RuCl_3$@PAN nanofibers were transformed into Ru@CNFs with numerous metallic Ru nanoparticles embedded in CNFs. Afterwards, the chalcogenation of Ru@CNFs was further carried out at 700 °C under an Ar atmosphere by placing S/Se/Te powder at the upstream side of the tube furnace. The sublimated S/Se/Te gas was reacted with Ru nanoparticles at the elevated temperature, which were respectively converted to RuS_2/$RuSe_2$/$RuTe_2$ nanoparticles.

Figure S1(a) in the Electronic Supplementary Material (ESM) shows the SEM image of $RuCl_3$@PAN, which displays continuous nanofibrous structure with an average diameter of around 300 nm. Figure S1(b) in the ESM shows the FT-IR spectra of $RuCl_3$@PAN, PAN, and $RuCl_3$. The FT-IR spectrum of $RuCl_3$@PAN is dominated by the feature peaks of PAN. An additional broad peak located at 1575 cm^{-1} appears arising from the feature peak of $RuCl_3$, indicating the successful doping of $RuCl_3$ into PAN matrix. Figure S2(a) in the ESM exhibits the XRD pattern of the carbonized sample Ru@CNFs. The sharp peaks located at 38.4°, 42.2°, and 44° are ascribed to the feature peaks of metallic Ru (JCPDS No. 06-0663), whereas the broad peak at around 25° is attributable to amorphous carbon-based material. SEM and TEM images of Ru@CNFs display the well-retained nanofibrous structure (Figs. S2(b) and S2(c) in the ESM), except that the nanofibers are slightly shrunk with the diameter of around 200 nm. Ultrafine Ru nanoparticles are homogeneous distributed in CNFs with the diameter of around 4 nm (Fig. S2(c) in the ESM), demonstrating the successful carbothermal reduction of $RuCl_3$ to metallic Ru nanoparticles.

Figure 1(a) shows the XRD patterns of RuX_2@CNFs samples obtained by the chalcogenation of Ru@CNFs at 700 °C. The XRD peaks of RuS_2@CNFs, $RuSe_2$@CNFs, and $RuTe_2$@CNFs are well-indexed to the pure-phase of RuS_2 (JCPDS No. 80-0669), $RuSe_2$ (JCPDS No. 80-0670), and $RuTe_2$ (JCPDS No. 88-1380), respectively, indicating the successful chalcogenation of metallic Ru to form RuX_2. In Fig. 1(b), the Raman spectra of RuX_2@CNFs samples all exhibit two broad peaks of CNFs with D (defect) band at around 1350 cm^{-1} and G (graphite) band at around 1600 cm^{-1}. The I_D/I_G peak intensity ratios of RuS_2@CNFs, $RuSe_2$@CNFs, and $RuTe_2$@CNFs are calculated as around 0.7, 0.8, and 0.84, respectively.

The chemical compositions and electronic states of RuX_2@CNFs samples were explored by XPS measurements. In Fig. S3 in the ESM, the XPS survey spectra of RuX_2@CNFs samples show the existence of C, N, O, Ru, and X elements. The high-resolution Ru 3p XPS spectra of RuX_2@CNFs samples exhibit the doublet peaks of Ru $3p_{1/2}$ and Ru $3p_{3/2}$ (Fig. 1(c)) [33]. As can be seen, the binding energies of Ru 3p peaks are gradually negatively shifted from RuS_2 to $RuSe_2$ and further to $RuTe_2$. The results indicate that Ru atoms in $RuTe_2$ possess a more negative charge (δ^-) than those in $RuSe_2$ and RuS_2, which are in accordance with the decrease of electronegativity from S to Se and further to Te [22]. The C 1s and N 1s XPS spectra of RuX_2@CNFs samples in Fig. S4 in the ESM reveal that N atoms have doped into carbon matrix in the form of pyridinic N, pyrrolic N, and graphitic N. The differences in the N 1s spectra of RuX_2@CNFs samples, especially for the area ratios of pyridinic N, pyrrolic N, and graphitic N, should be caused along with the different chalcogenation processes. Figure 1(d) shows the S 2p XPS spectra of RuS_2@CNFs. The doublet peaks at 162.8 and 163.8 eV are ascribed to S $2p_{3/2}$ and S $2p_{1/2}$ peaks of Ru–S bond in RuS_2, respectively. The peaks at 164 and 165.1 eV are attributed to the bonding state of C–S–C, implying that partial S atoms have doped into the carbon matrix [34]. The existence of S–O bond is owing to the unavoidable surface oxidation under ambient condition. In Fig. 1(e), the Se 3d XPS spectra of $RuSe_2$@CNFs show the dominant peaks at 54.9 and 55.8 eV, which are indexed to Se $3d_{5/2}$ and Se $3d_{3/2}$ peaks of Ru–Se bond in $RuSe_2$, respectively. In addition, the existence of Se–O bond is caused by the surface oxidation [28]. In Fig. 1(f), the Te 3d XPS spectra of $RuTe_2$@CNFs can be deconvolved into four peaks. The dominant doublet peaks at 573.3 and 583.7 eV are Te $3d_{5/2}$ and Te $3d_{3/2}$ peaks arising from the bonding state of Ru–Te, whereas another doublet peaks at 576.1 and 586.4 eV are ascribed to Te–O that formed by surface oxidation [29].

The morphologies of RuX_2@CNFs samples were characterized by SEM and TEM. As shown in Figs. 2(a)–2(c), SEM images of RuX_2@CNFs samples all exhibit the well-maintained nanofibrous structures with an average diameter of around 150 nm. The nanofibers are interconnected with each other to form a porous nonwoven structure (Fig. S5 in the ESM), which is beneficial for electrolyte penetration and gas emission [32]. In Fig. S6 in the ESM, the EDX spectra of RuX_2@CNFs samples reveal the elemental compositions of C, N, O, Ru, and X, which are consistent with the results of XPS. In Figs. 2(d)–2(f) in the ESM, TEM images of RuX_2@CNFs samples reveal that numerous RuX_2 nanoparticles are uniformly distributed in the carbon matrix. Notably, RuS_2@CNFs show a smaller RuX_2 nanoparticle size of around 10 nm than $RuSe_2$@CNFs (around 30 nm) and $RuTe_2$@CNFs (around 20 nm). The results indicate that the nanoparticle size of RuX_2 is highly dependent on the different chalcogenation treatments, and the smaller size of RuS_2 is expected to expose more catalytic active sites. In Figs. 2(g)–2(i), and Fig. S7 in the ESM, the HRTEM images of RuX_2@CNFs samples exhibit the lattice fringes with *d*-spacings of 0.32, 0.34, and 0.28 nm for RuX_2 nanoparticles, which are consistent with the (111) crystal planes of RuS_2, $RuSe_2$, and $RuTe_2$, respectively. In summary, the aforementioned FT-IR, XRD, Raman, XPS, SEM, and TEM characterization results demonstrate the successful fabrication of RuX_2@CNFs samples, consisting of numerous RuX_2 nanoparticles with exposed (111) crystal planes that are uniformly embedded on

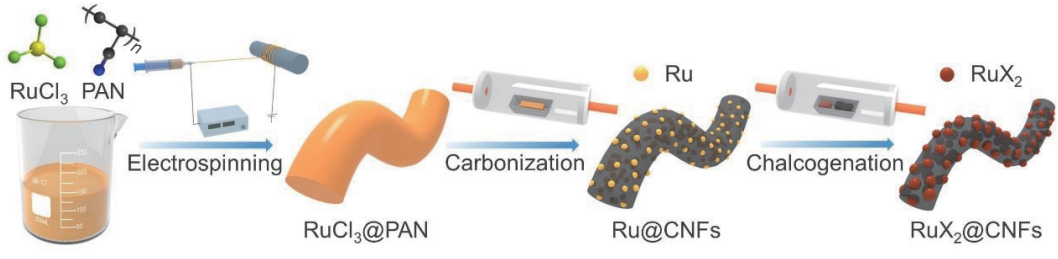

Scheme 1 Schematic illustration of the synthesis for RuX_2@CNFs (X = S/Se/Te).

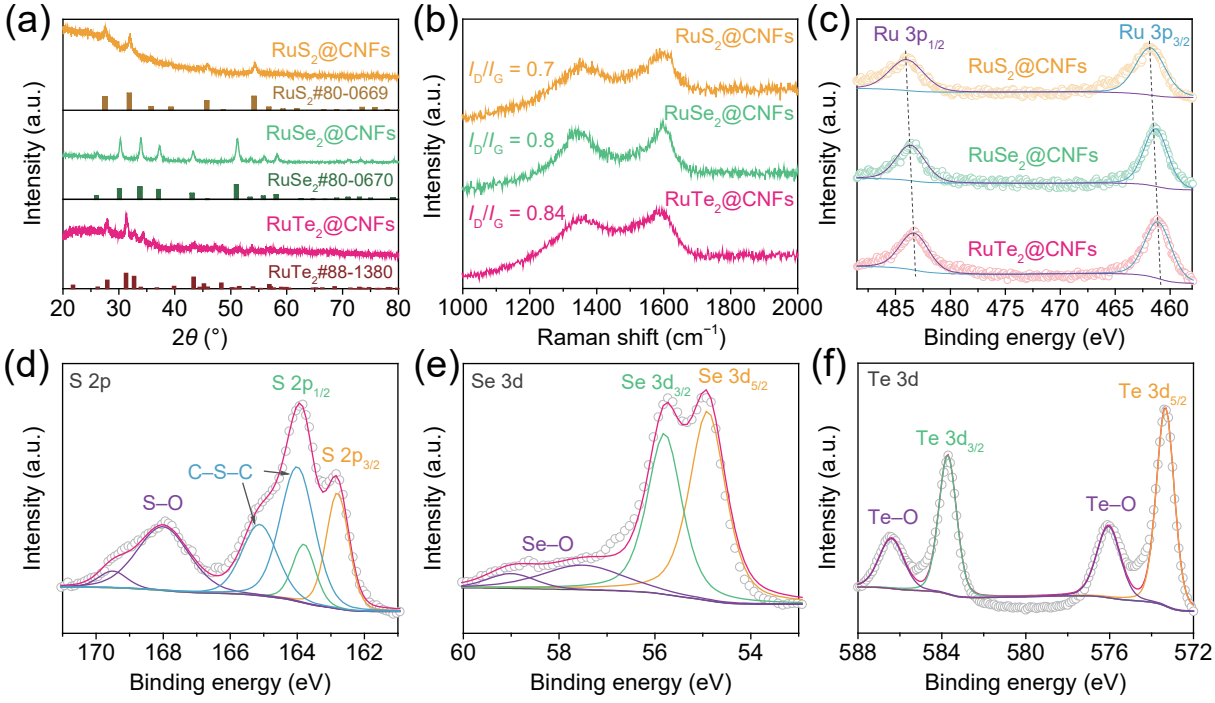

Figure 1 (a) XRD patterns, (b) Raman spectra, and (c) high-resolution Ru 3p XPS spectra of RuS_2@CNFs, $RuSe_2$@CNFs, and $RuTe_2$@CNFs. High-resolution XPS spectra of (d) S 2p of RuS_2@CNFs, (e) Se 3d of $RuSe_2$@CNFs, and (f) Te 3d of $RuTe_2$@CNFs.

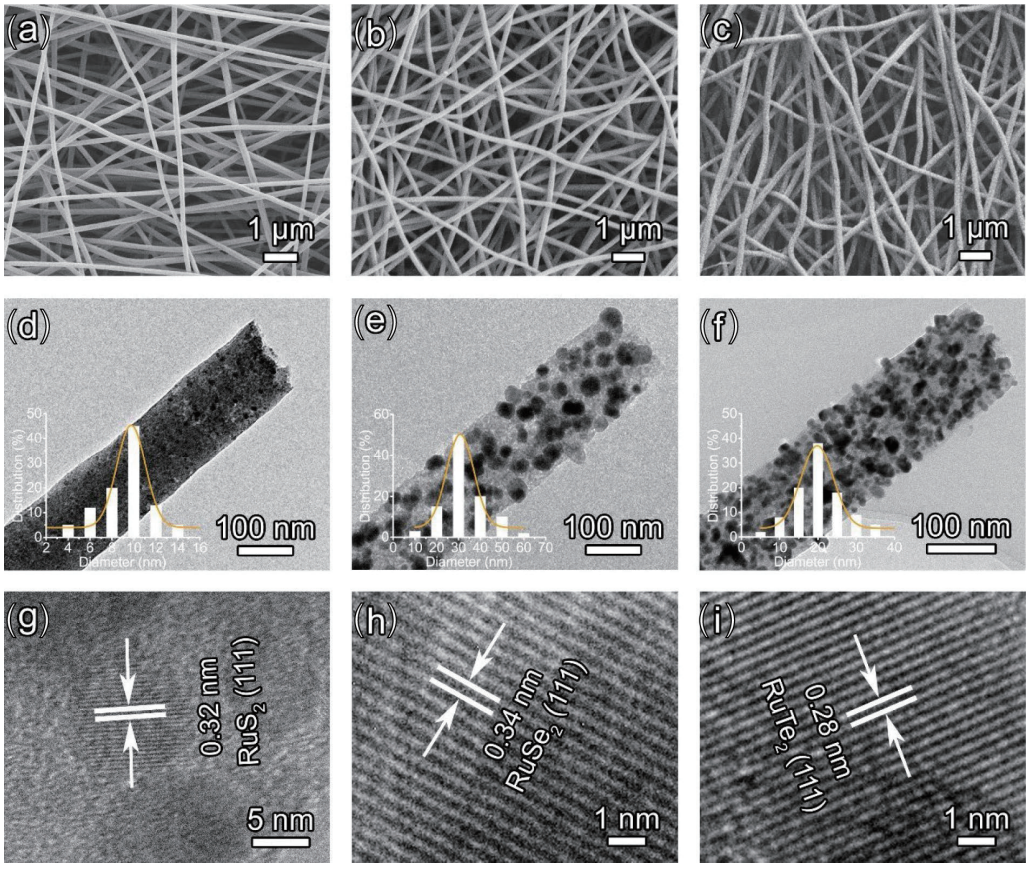

Figure 2 ((a)–(c)) SEM, ((d)–(f)) TEM, and ((g)–(i)) HRTEM images of ((a), (d), and (g)) RuS_2@CNFs, ((b), (e), and (h)) $RuSe_2$@CNFs, and ((c), (f), and (i)) $RuTe_2$@CNFs. Insets in ((d)–(f)) are the related distribution histogram of the diameter of RuX_2 nanoparticles.

CNFs. The CNFs acted as conductive substrate are of importance in avoiding the aggregation of RuX_2 nanoparticles and enabling the rapid electron transfer for accelerated electrocatalysis [31]. The N_2 adsorption–desorption isotherms of RuX_2@CNFs samples are shown in Fig. S8 in the ESM. The BET specific surface areas of RuS_2@CNFs, $RuSe_2$@CNFs, and $RuTe_2$@CNFs are calculated as 186.7, 120, and 137.7 $m^2 \cdot g^{-1}$, respectively.

3.2 HER catalytic performances of the RuX_2@CNFs catalysts

The HER catalytic performances of the RuX_2@CNFs catalysts were first evaluated in 0.5 M H_2SO_4 by using a typical three-electrode setup. For comparison, the reference sample of commercial 20% Pt/C was also measured under the identical

experimental conditions. LSV curves of RuX_2@CNFs and 20% Pt/C in 0.5 M H_2SO_4 are shown in Fig. 3(a). The commercial 20% Pt/C shows the highest HER catalytic performance in acidic media, whereas RuS_2@CNFs exhibit a higher HER catalytic performance than $RuSe_2$@CNFs and $RuTe_2$@CNFs. To achieve a current density of 10 mA·cm^{-2}, the required overpotentials (η_{10}) are 12, 44, 59, and 79 mV for 20% Pt/C, RuS_2@CNFs, $RuSe_2$@CNFs, and $RuTe_2$@CNFs, respectively. In Fig. 3(b), the corresponding Tafel plots display the lowest Tafel slope of 35.6 mV·dec^{-1} for 20% Pt/C. For the RuX_2@CNFs catalysts, RuS_2@CNFs show a lower Tafel slope of 44.3 mV·dec^{-1} than $RuSe_2$@CNFs (47.8 mV·dec^{-1}) and $RuTe_2$@CNFs (56.1 mV·dec^{-1}), indicating the more favorable catalytic kinetic for RuS_2@CNFs. The exchange current densities (j_0) of the catalysts are shown in Fig. 3(c), which are calculated by extrapolating from the Tafel plots. For the RuX_2@CNFs catalysts, RuS_2@CNFs possess a highest j_0 value of 1.02 mA·cm^{-2}, followed by $RuSe_2$@CNFs (0.55 mA·cm^{-2}) and $RuTe_2$@CNFs (0.4 mA·cm^{-2}).

To estimate the ECSA, the C_{dl} values of the RuX_2@CNFs catalysts in 0.5 M H_2SO_4 were measured. Figures S9(a)–S9(c) in the ESM show the CV curves of the RuX_2@CNFs catalysts within the potential range of 0–0.2 V vs. RHE at different scan rates. The C_{dl} values of RuS_2@CNFs, $RuSe_2$@CNFs, and $RuTe_2$@CNFs are calculated as 200.6, 149, and 165.5 mF·cm^{-2} (Fig. S9(d) in the ESM), respectively. The results indicate a larger ECSA and thus more abundant catalytic active sites for RuS_2@CNFs. To make a specific HER catalytic activity comparison, LSV curves of the RuX_2@CNFs samples were normalized by ECSA. As shown in Fig. S10 in the ESM, the ECSA-normalized LSV curves confirm the catalytic activity order of RuS_2@CNFs > $RuSe_2$@CNFs > $RuTe_2$@CNFs, demonstrating the highest intrinsic catalytic activity for RuS_2@CNFs in 0.5 M H_2SO_4. In addition, EIS measurements were conducted to gain further insights into the HER catalytic kinetics of the RuX_2@CNFs catalysts in 0.5 M H_2SO_4. Nyquist plots in Fig. S11 in the ESM demonstrate that RuS_2@CNFs display a lower charge transfer resistance than $RuSe_2$@CNFs and $RuTe_2$@CNFs, confirming the superior HER catalytic kinetic of the former.

The HER catalytic performances of the RuX_2@CNFs catalysts and 20% Pt/C were also examined in 1 M KOH. Figure 3(d) shows the LSV curves of the samples in 1 M KOH. Due to the sluggish water dissociation ability of Pt in alkaline media, 20% Pt/C shows a seriously decreased HER catalytic activity in 1 M KOH compared with that in 0.5 M H_2SO_4. For the RuX_2@CNFs catalysts, however, their HER catalytic performances in 1 M KOH are all significantly higher than those in 0.5 M H_2SO_4. The η_{10} values are 33, 9, 32, and 16 mV for 20% Pt/C, RuS_2@CNFs, $RuSe_2$@CNFs, and $RuTe_2$@CNFs, respectively, revealing the higher HER catalytic performances of the RuX_2@CNFs catalysts than 20% Pt/C. In 1 M KOH, RuS_2@CNFs are still the best HER catalyst among the RuX_2@CNFs catalysts, but $RuTe_2$@CNFs show a higher HER catalytic performance than $RuSe_2$@CNFs. As a result, the catalytic performance sequence in alkaline media is different from that in acidic media, which is possibly associated with the media (pH) dependent elementary steps toward HER electrocatalysis. The Tafel plots in Fig. 3(e) demonstrate the lower Tafel slope of RuS_2@CNFs (35.7 mV·dec^{-1}) than $RuTe_2$@CNFs (38.8 mV·dec^{-1}) and $RuSe_2$@CNFs (45.7 mV·dec^{-1}), confirming the superior catalytic kinetic for RuS_2@CNFs. The calculated j_0 value of RuS_2@CNFs is 5.62 mA·cm^{-2} (Fig. 3(f)), which is higher than that of $RuTe_2$@CNFs (3.72 mA·cm^{-2}), 20% Pt/C (3.09 mA·cm^{-2}), and $RuSe_2$@CNFs (2 mA·cm^{-2}). The specific HER catalytic activity comparison was further conducted by ECSA-normalizing the LSV curves (Figs. S12 and S13 in the ESM), which confirmed the catalytic activity order of RuS_2@CNFs > $RuTe_2$@CNFs > $RuSe_2$@CNFs in 1 M KOH.

On the basis of the above results, the order of catalytic performance is RuS_2@CNFs > $RuSe_2$@CNFs > $RuTe_2$@CNFs in acidic media, whereas it is changed to RuS_2@CNFs > $RuTe_2$@CNFs > $RuSe_2$@CNFs in alkaline media. Among the RuX_2@CNFs catalysts, RuS_2@CNFs show the highest catalytic performance in both acidic and alkaline media. Remarkably, the HER catalytic performance of RuS_2@CNFs is also superior to a majority of the recently reported Ru-based electrocatalysts in acidic and alkaline media (Tables S1 and S2 in the ESM).

Given that the superior catalytic activity of RuS_2@CNFs, the effects of $RuCl_3$ feeding content and sulfuration temperature, on the nature of the products and their catalytic performances, were further investigated (Figs. S14–S19 in the ESM). In addition to the RuS_2@CNFs sample, obtained with $RuCl_3$ feeding content of

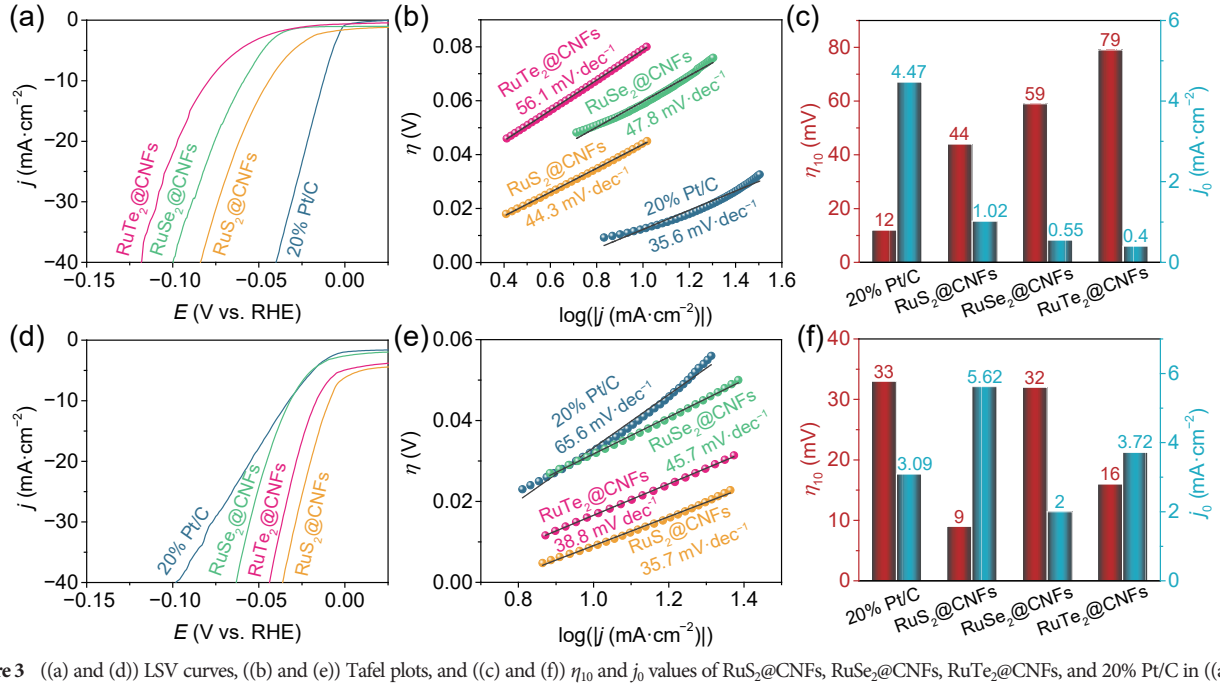

Figure 3 ((a) and (d)) LSV curves, ((b) and (e)) Tafel plots, and ((c) and (f)) η_{10} and j_0 values of RuS_2@CNFs, $RuSe_2$@CNFs, $RuTe_2$@CNFs, and 20% Pt/C in ((a)–(c)) 0.5 M H_2SO_4 and ((d)–(f)) 1 M KOH.

0.5 mmol and at a sulfuration temperature of 700 °C, four additional reference samples were obtained with $RuCl_3$ feeding contents of 0.25 and 1 mmol or under sulfuration temperatures of 600 and 800 °C. The characterization results demonstrate that the composition and morphology of the reference samples are generally identical to the RuS_2@CNFs sample, except for the differences in the loading content, the nanoparticle size of RuS_2, and the diameter of CNFs. With an increase of $RuCl_3$ feeding content, the RuS_2 loading content and CNFs diameter of the resultant catalysts are both increased. When increasing the sulfuration temperature, RuS_2 nanoparticles are gradually aggregated, and the CNFs are fractured at an elevated temperature of 800 °C. After evaluating the HER catalytic performances of these samples in 0.5 M H_2SO_4 and 1 M KOH, the optimal RuS_2@CNFs sample should be synthesized with $RuCl_3$ feeding content of 0.5 mmol and at a sulfuration temperature of 700 °C.

The HER catalytic durability of RuS_2@CNFs was evaluated by continuous CV scanning within the potential range of −0.1–0.1 V vs. RHE and long-term electrolysis at the applied overpotentials. As shown in Fig. S20 in the ESM, the LSV curves were hardly altered after 3000 CV cycles, and the HER catalytic current densities were well-maintained after the long-term electrolysis in both 0.5 M H_2SO_4 and 1 M KOH. The results demonstrate the excellent catalytic stability of RuS_2@CNFs in acidic and alkaline media. In addition, the post-electrolysis XRD characterizations reveal the well-preserved crystalline phase of RuS_2 (Fig. S21 in the ESM), which confirms its high structural stability during the HER electrocatalysis.

3.3 DFT calculations

Comprehensive DFT calculations were conducted to provide deep insights into the chalcogen-dependent catalytic properties of RuX_2. Reasonable structure models of RuS_2 (111), $RuSe_2$ (111), and $RuTe_2$ (111) were constructed in line with the identical exposed crystal planes of RuX_2 (111) in HRTEM images (Fig. S22 in the ESM). According to Sabatier principle, the Gibbs free energy of hydrogen adsorption (ΔG_{H^*}) was generally used to evaluate the relative HER catalytic activity in acidic media. A decrease in $|\Delta G_{H^*}|$ value indicates an increase in HER catalytic activity [35]. Figures 4(a)–4(c) show the schematic models of RuS_2 (111), $RuSe_2$ (111), and $RuTe_2$ (111) with an absorbed hydrogen atom (H^*) at their optimal sites (Ru sites). In Fig. 4(d), the calculated ΔG_{H^*} values of RuS_2 (111), $RuSe_2$ (111), and $RuTe_2$ (111) are 0.11, 0.17, and 0.18 eV, respectively, implying the highest intrinsic HER catalytic activity for RuS_2 (111). The results of calculated ΔG_{H^*} values are consistent with the experimental catalytic activity order of RuS_2@CNFs > $RuSe_2$@CNFs > $RuTe_2$@CNFs in acidic media.

In alkaline media, the HER process involves several elementary steps, including adsorption of H_2O, dissociation of H_2O, desorption of OH^-, and desorption of generated H_2 [36]. Therefore, the optimized Gibbs free energy diagrams of the elementary steps for alkaline HER electrocatalysis were also calculated. As shown in Fig. 4(e), RuS_2 (111) shows an ultralow H_2O dissociation barrier of 0.01 eV to achieve rapid proton formation in alkaline media. Compared to $RuSe_2$ (111) with a higher H_2O dissociation barrier of 0.74 eV, $RuTe_2$ (111) exhibits a lower H_2O dissociation barrier of 0.51 eV indicating its more favorable H_2O dissociation process. Besides H_2O dissociation, the OH^- desorption barriers for RuS_2 (111), $RuSe_2$ (111), and $RuTe_2$ (111) are also calculated as 0.74, 1.52, and 1.15 eV, respectively, demonstrating that the rate-determining step for RuX_2 (111) is the desorption of OH^- in alkaline media. The lowest energy barrier for RuS_2 (111) indicates the most facilitated OH^- desorption, which is highly desirable to release more catalytic active sites by alleviating the site-blocking effect from strong OH^- absorption [36]. In addition, the DFT calculation analysis is in good agreement with

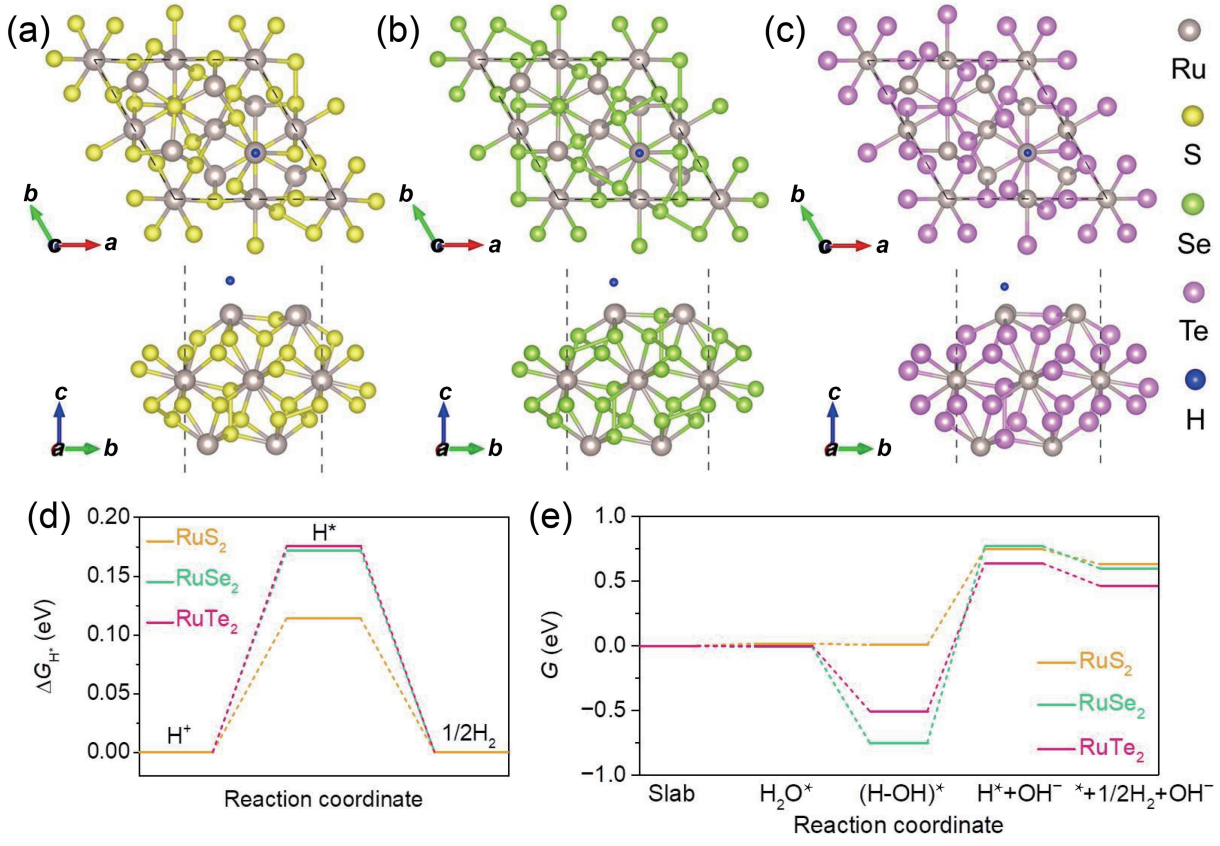

Figure 4 Top and side views of schematic models for (a) RuS_2 (111), (b) $RuSe_2$ (111), and (c) $RuTe_2$ (111) with an absorbed hydrogen atom at their optimal catalytic active sites. (d) Calculated ΔG_{H^*} values for RuS_2 (111), $RuSe_2$ (111), and $RuTe_2$ (111). (e) Free energy diagrams of the elementary steps in alkaline HER for RuS_2 (111), $RuSe_2$ (111), and $RuTe_2$ (111).

the experimental results with the alkaline catalytic activity order of RuS_2@CNFs > $RuTe_2$@CNFs > $RuSe_2$@CNFs. The schematic illustrations of the HER electrocatalysis for RuX_2 (111) are shown in Figs. S23–S25 in the ESM.

To get further insights into the electronic structures of RuX_2, the band structures of RuS_2, $RuSe_2$, and $RuTe_2$ were calculated. Figures 5(a)–5(c) show the crystal structure models for RuS_2, $RuSe_2$, and $RuTe_2$. In Figs. 5(d)–5(f), the band gaps for RuS_2, $RuSe_2$, and $RuTe_2$ are calculated as 0.63, 0.32, and 0.11 eV, respectively. The smaller band gap of $RuTe_2$ is expected to possess the higher conductivity. In Fig. 5(g), the density of states (DOS) for RuX_2 demonstrates that $RuTe_2$ possesses higher electron density near Fermi level (E_F) than $RuSe_2$ and RuS_2. Further partial density of states (PDOS) analysis suggests that the DOS near E_F of $RuTe_2$ is mainly from Ru; nevertheless, the participation of Te also plays a crucial role in increasing the carrier density for $RuTe_2$ near E_F and enhance the conductivity (Fig. 5(h)). Consistent with the DOS analysis, the calculated electronic conductivity in Fig. 5(i) demonstrates the conductivity order of $RuTe_2$ > $RuSe_2$ > RuS_2.

Although RuS_2 possesses the relative lower conductivity, RuS_2@CNFs still exhibit the highest catalytic activity among RuX_2@CNFs samples in both acidic and alkaline media. The results can be attributed to the following reasons. (i) The chalcogen-dependent catalytic properties of RuX_2 should play the dominant role in the HER catalytic activity. Among RuX_2 samples, RuS_2 (111) shows the lowest reaction barriers and the highest intrinsic catalytic activity in both acidic and alkaline media. (ii) RuX_2@CNFs consisted of numerous RuX_2 nanoparticles that are uniformly distributed in the highly conductive CNFs. Compared with $RuSe_2$@CNFs and $RuTe_2$@CNFs, RuS_2@CNFs show a smaller nanoparticle size of RuX_2 and thereby more contact area with conductive carbon matrix, which may offset the conductivity limitation of RuS_2 to a great extent.

4 Conclusions

In summary, a series of RuX_2 (X = S/Se/Te) nanoparticles decorated carbon nanofibers were successfully fabricated via a facile electrospinning-assisted synthetic strategy. The identical nanofibrous morphologies and the specific exposed crystal faces of RuX_2 (111) pave the way to make a fair and direct comparison for the HER catalytic activities of RuX_2@CNFs. In 0.5 M H_2SO_4, RuS_2@CNFs show the highest HER catalytic activity, followed by $RuSe_2$@CNFs and then $RuTe_2$@CNFs. In 1 M KOH, however, the order of catalytic activity is changed to RuS_2@CNFs > $RuTe_2$@CNFs > $RuSe_2$@CNFs. Comprehensive DFT calculations were conducted to reveal the highest intrinsic catalytic activity of RuS_2 (111) by analyzing the HER energy barriers. The altered catalytic activity sequences for $RuSe_2$ (111) and $RuTe_2$ (111) are attributable to their varied catalytic properties for the different elementary steps during the acidic and alkaline HER electrocatalysis. $RuSe_2$ (111) shows the superior ΔG_{H^*} value to $RuTe_2$ (111) in 0.5 M H_2SO_4, whereas $RuTe_2$ (111) shows enhanced catalytic property for H_2O dissociation and OH^- desorption than $RuSe_2$ (111) in 1 M KOH. Although the conductivity of RuX_2 follows the order of $RuTe_2$ > $RuSe_2$ > RuS_2,

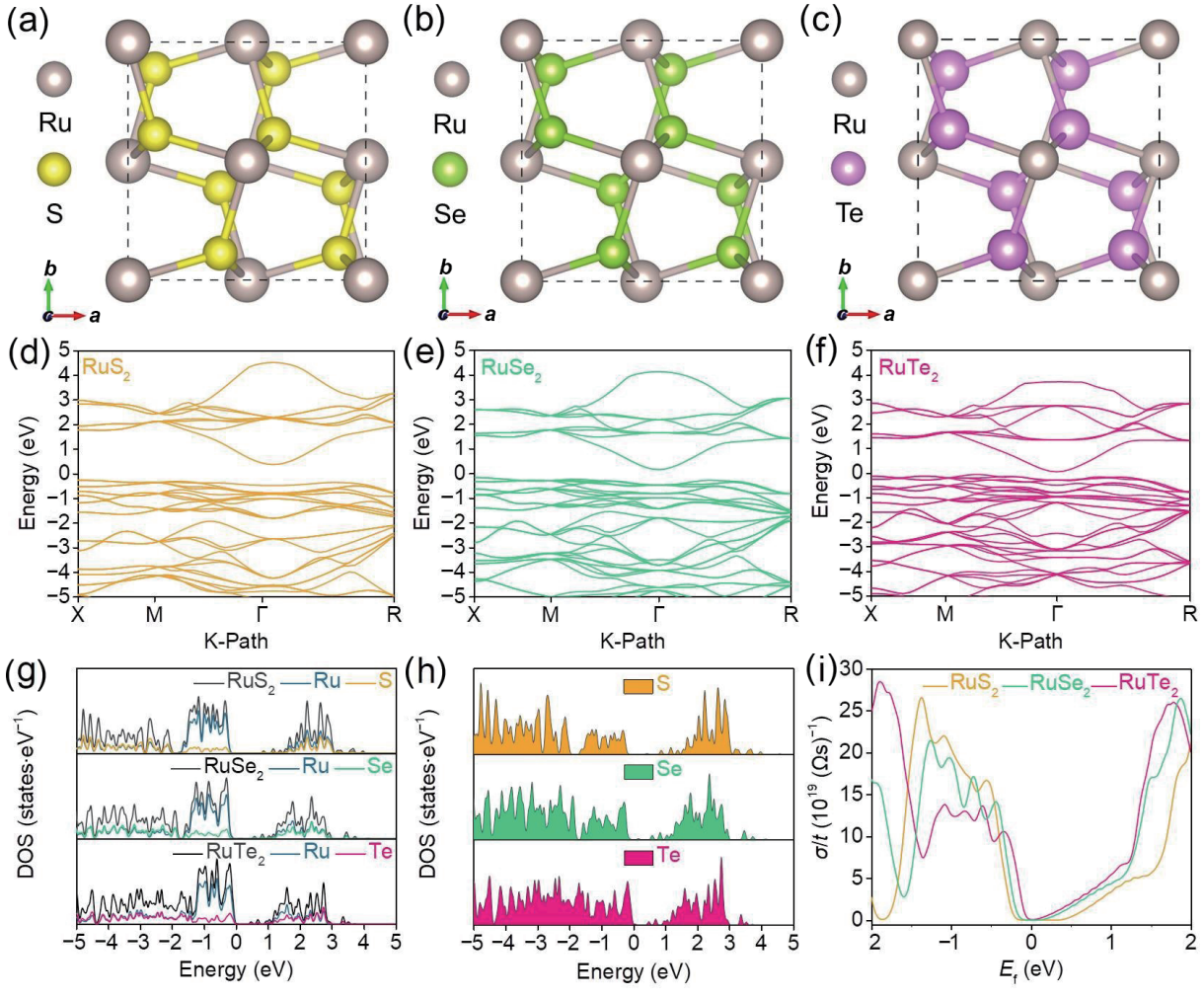

Figure 5 ((a)–(f)) The crystal structure models and corresponding electronic-band structures for ((a) and (d)) RuS_2, ((b) and (e)) $RuSe_2$, and ((c) and (f)) $RuTe_2$. (g) The electronic density of states calculated for RuS_2, $RuSe_2$, and $RuTe_2$. (h) The partial (S, Se, and Te) electronic density of states calculated for RuS_2, $RuSe_2$, and $RuTe_2$. (i) The calculated electronic conductivity for RuS_2, $RuSe_2$, and $RuTe_2$.

the relative higher intrinsic catalytic activity of RuS_2 (111) should play the dominant role to achieve the highly efficient HER electrocatalysis on RuS_2@CNFs. This study provides fundamental insights for understanding the chalcogen-dependent intrinsic catalytic properties of RuX_2 with specific exposed crystal planes in acidic and alkaline media, motivating the further comparative investigation of other noble-metal (such as Rh, Pd, Os, and Ir) based sulfides, selenides, and tellurides toward HER electrocatalysis and beyond.

Acknowledgements

This work was financially supported by Natural Science Foundation of Zhejiang Province (Nos. LQ20B030001 and LZ22C100002) and China Postdoctoral Science Foundation (No. 2021M702305).

Electronic Supplementary Material: Supplementary material (further detailed SEM images, FT-IR spectra, XRD patterns, TEM images, XPS spectra, EDX spectra, BET measurements, Raman spectra, CV curves, LSV curves, Tafel plots, Nyquist plots, electrolysis curves, and schematic models) is available in the online version of this article at https://doi.org/10.1007/s12274-023-6206-9.

References

[1] Yang, Y. X.; Li, P.; Zheng, X. B.; Sun, W. P.; Dou, S. X.; Ma, T. Y.; Pan, H. G. Anion-exchange membrane water electrolyzers and fuel cells. *Chem. Soc. Rev.* **2022**, *51*, 9620–9693.

[2] Chatenet, M.; Pollet, B. G.; Dekel, D. R.; Dionigi, F.; Deseure, J.; Millet, P.; Braatz, R. D.; Bazant, M. Z.; Eikerling, M.; Staffell, I. et al. Water electrolysis: From textbook knowledge to the latest scientific strategies and industrial developments. *Chem. Soc. Rev.* **2022**, *51*, 4583–4762.

[3] Yan, D. F.; Mebrahtu, C.; Wang, S. Y.; Palkovits, R. Innovative electrochemical strategies for hydrogen production: From electricity input to electricity output. *Angew. Chem., Int. Ed.* **2023**, *62*, e202214333.

[4] Li, J. W.; Yin, W. N.; Pan, J. N.; Zhang, Y. B.; Wang, F. S.; Wang, L. L.; Zhao, Q. External field assisted hydrogen evolution reaction. *Nano Res.* **2023**, *16*, 8638–8654.

[5] Wan, L.; Xu, Z. A.; Xu, Q.; Pang, M. B.; Lin, D. C.; Liu, J.; Wang, B. G. Key components and design strategy of the membrane electrode assembly for alkaline water electrolysis. *Energy Environ. Sci.* **2023**, *16*, 1384–1430.

[6] Zhang, W. Z.; Liu, M. H.; Gu, X.; Shi, Y. X.; Deng, Z. F.; Cai, N. S. Water electrolysis toward elevated temperature: Advances, challenges, and frontiers. *Chem. Rev.* **2023**, *123*, 7119–7192.

[7] Liu, J. Y.; Duan, S.; Shi, H.; Wang, T. Y.; Yang, X. X.; Huang, Y. H.; Wu, G.; Li, Q. Rationally designing efficient electrocatalysts for direct seawater splitting: Challenges, achievements, and promises. *Angew. Chem., Int. Ed.* **2022**, *61*, e202210753.

[8] Fu, X. W.; Shi, R. J.; Jiao, S. L.; Li, M. M.; Li, Q. Y. Structural design for electrocatalytic water splitting to realize industrial-scale deployment: Strategies, advances, and perspectives. *J. Energy Chem.* **2022**, *70*, 129–153.

[9] Barrio, J.; Pedersen, A.; Favero, S.; Luo, H.; Wang, M. N.; Sarma, S. C.; Feng, J. Y.; Ngoc, L. T. T.; Kellner, S.; Li, A. Y. et al. Bioinspired and bioderived aqueous electrocatalysis. *Chem. Rev.* **2023**, *123*, 2311–2348.

[10] Zhao, H.; Yuan, Z. Y. Progress and perspectives for solar-driven water electrolysis to produce green hydrogen. *Adv. Energy Mater.* **2023**, *13*, 2300254.

[11] Zhai, Y. Y.; Ren, X. R.; Wang, B. L.; Liu, S. Z. High-entropy catalyst-a novel platform for electrochemical water splitting. *Adv. Funct. Mater.* **2022**, *32*, 2207536.

[12] Guo, F.; Macdonald, T. J.; Sobrido, A. J.; Liu, L. X.; Feng, J. R.; He, G. J. Recent advances in ultralow-Pt-loading electrocatalysts for the efficient hydrogen evolution. *Adv. Sci.* **2023**, *10*, 2301098.

[13] Cui, Z. B.; Jiao, W. S.; Huang, Z. Y.; Chen, G. Z.; Zhang, B.; Han, Y. H.; Huang, W. Design and synthesis of noble metal-based alloy electrocatalysts and their application in hydrogen evolution reaction. *Small* **2023**, *19*, 2301465.

[14] Shit, S.; Bolar, S.; Murmu, N. C.; Kuila, T. An account of the strategies to enhance the water splitting efficiency of noble-metal-free electrocatalysts. *J. Energy Chem.* **2021**, *59*, 160–190.

[15] Jin, M. T.; Zhang, X.; Niu, S. Z.; Wang, Q.; Huang, R. Q.; Ling, R. H.; Huang, J. Q.; Shi, R.; Amini, A.; Cheng, C. Strategies for designing high-performance hydrogen evolution reaction electrocatalysts at large current densities above 1000 $mA \cdot cm^{-2}$. *ACS Nano* **2022**, *16*, 11577–11597.

[16] Luo, Y. T.; Zhang, Z. Y.; Chhowalla, M.; Liu, B. L. Recent advances in design of electrocatalysts for high-current-density water splitting. *Adv. Mater.* **2022**, *34*, 2108133.

[17] Xiong, L. W.; Qiu, Y. F.; Peng, X.; Liu, Z. T.; Chu, P. K. Electronic structural engineering of transition metal-based electrocatalysts for the hydrogen evolution reaction. *Nano Energy* **2022**, *104*, 107882.

[18] Xia, H.; Shi, Z. D.; Gong, C. S.; He, Y. M. Recent strategies for activating the basal planes of transition metal dichalcogenides towards hydrogen production. *J. Mater. Chem. A* **2022**, *10*, 19067–19089.

[19] Kirubasankar, B.; Won, Y. S.; Adofo, L. A.; Choi, S. H.; Kim, S. M.; Kim, K. K. Atomic and structural modifications of two-dimensional transition metal dichalcogenides for various advanced applications. *Chem. Sci.* **2022**, *13*, 7707–7738.

[20] Mondal, A.; Vomiero, A. 2D transition metal dichalcogenides-based electrocatalysts for hydrogen evolution reaction. *Adv. Funct. Mater.* **2022**, *32*, 2208994.

[21] Chia, X. Y.; Ambrosi, A.; Lazar, P.; Sofer, Z.; Pumera, M. Electrocatalysis of layered group 5 metallic transition metal dichalcogenides (MX_2, M = V, Nb, and Ta; X = S, Se, and Te). *J. Mater. Chem. A* **2016**, *4*, 14241–14253.

[22] Ge, Y. C.; Gao, S. P.; Dong, P.; Baines, R.; Ajayan, P. M.; Ye, M. X.; Shen, J. F. Insight into the hydrogen evolution reaction of nickel dichalcogenide nanosheets: Activities related to non-metal ligands. *Nanoscale* **2017**, *9*, 5538–5544.

[23] Li, J.; Hong, M. L.; Sun, L. J.; Zhang, W. F.; Shu, H. B.; Chang, H. X. Enhanced electrocatalytic hydrogen evolution from large-scale, facile-prepared, highly crystalline WTe_2 nanoribbons with weyl semimetallic phase. *ACS Appl. Mater. Interfaces* **2018**, *10*, 458–467.

[24] Bhat, K. S.; Nagaraja, H. S. Performance evaluation of molybdenum dichalcogenide (MoX_2; X= S, Se, Te) nanostructures for hydrogen evolution reaction. *Int. J. Hydrogen Energy* **2019**, *44*, 17878–17886.

[25] Yang, Y. J.; Yu, Y. H.; Li, J.; Chen, Q. R.; Du, Y. L.; Rao, P.; Li, R. S.; Jia, C. M.; Kang, Z. Y.; Deng, P. L. et al. Engineering ruthenium-based electrocatalysts for effective hydrogen evolution reaction. *Nano-Micro Lett.* **2021**, *13*, 160.

[26] Ma, R. P.; Wang, X.; Yang, X. L.; Li, Y.; Liu, C. P.; Ge, J. J.; Xing, W. Identification of active sites and synergistic effect in multicomponent carbon-based Ru catalysts during electrocatalytic hydrogen evolution. *Nano Res.* **2022**, *16*, 166–173.

[27] Zhu, J. W.; Guo, Y.; Liu, F.; Xu, H. W.; Gong, L.; Shi, W. J.; Chen, D.; Wang, P. Y.; Yang, Y.; Zhang, C. T. et al. Regulative electronic states around ruthenium/ruthenium disulphide heterointerfaces for efficient water splitting in acidic media. *Angew. Chem., Int. Ed.* **2021**, *60*, 12328–12334.

[28] Zhao, Y. M.; Cong, H. J.; Li, P.; Wu, D. A.; Chen, S. L.; Luo, W. Hexagonal $RuSe_2$ nanosheets for highly efficient hydrogen evolution electrocatalysis. *Angew. Chem., Int. Ed.* **2021**, *60*, 7013–7017.

[29] Tang, B.; Yang, X. D.; Kang, Z. H.; Feng, L. G. Crystallized $RuTe_2$ as unexpected bifunctional catalyst for overall water splitting. *Appl. Catal. B Environ.* **2020**, *278*, 119281.

[30] Zhang, Z.; Jiang, C.; Li, P.; Yao, K. G.; Zhao, Z. L.; Fan, J. T.; Li, H.; Wang, H. J. Benchmarking phases of ruthenium dichalcogenides for electrocatalysis of hydrogen evolution: Theoretical and experimental insights. *Small* **2021**, *17*, 2007333.

[31] Cao, X. J.; Wang, T. Z.; Jiao, L. F. Transition-metal (Fe, Co, and Ni)-based nanofiber electrocatalysts for water splitting. *Adv. Fiber Mater.* **2021**, *3*, 210–228.
[32] Zhang, F. Z.; Chen, J.; Yang, J. P. Fiber materials for electrocatalysis applications. *Adv. Fiber Mater.* **2022**, *4*, 720–735.
[33] Wei, Y.; Xu, G.; Wei, Y. J.; Ji, L.; Wang, T.; Liu, Z.; Wang, S. Temperature-controlled synthesis of heterostructured Ru-Ru_2P nanoparticles embedded in carbon nanofibers for highly efficient hydrogen production. *Sci. China Mater.* **2022**, *65*, 2675–2684.
[34] Ito, Y.; Cong, W. T.; Fujita, T.; Tang, Z.; Chen, M. W. High catalytic activity of nitrogen and sulfur co-doped nanoporous graphene in the hydrogen evolution reaction. *Angew. Chem., Int. Ed.* **2015**, *54*, 2131–2136.
[35] Nørskov, J. K.; Bligaard, T.; Logadottir, A.; Kitchin, J. R.; Chen, J. G.; Pandelov, S.; Stimming, U. Trends in the exchange current for hydrogen evolution. *J. Electrochem. Soc.* **2005**, *152*, J23–J26.
[36] He, Q.; Zhou, Y. Z.; Shou, H. W.; Wang, X. Y.; Zhang, P. J.; Xu, W. J.; Qiao, S. C.; Wu, C. Q.; Liu, H. J.; Liu, D. B. et al. Synergic reaction kinetics over adjacent ruthenium sites for superb hydrogen generation in alkaline media. *Adv. Mater.* **2022**, *34*, 2110604.